

# Abstract

The system under development will combine elements of fringe projection and line scanning to create a rapid, high-resolution method for scanning entire three-dimensional components of a wide range of sizes. Projecting sinusoidal fringes on a rotating subject will yield a rapid approximation of a three-dimensional object; this approximation will then be used to combine the results of a more thorough fringe-projection scan to obtain high resolutions. Such a technique yields all of the benefits of fringe-projection without the need to perform time-consuming calculations such as phase unwrapping or point cloud stitching.

The system's generated object geometry will be compatible with all major CAD packages, allowing for true reverse-engineering in one step. The ability to modify and rapid-prototype a version of the original part will greatly streamline the product development process.

# Contents

<b>1</b>	<b>Background</b>	<b>2</b>
1.1	3-Dimensional Optical Shape Measurement Techniques . . . . .	2
1.1.1	Photogrammetry . . . . .	2
1.1.2	Time of Flight . . . . .	3
1.1.3	Triangulation . . . . .	3
1.1.3.1	Laser Scanning . . . . .	3
1.1.3.2	Structured Light . . . . .	4
1.1.4	Interferometry . . . . .	8
1.2	Existing Commercial Products . . . . .	8
1.2.0.1	Kinect . . . . .	8
1.2.0.2	Next Engine . . . . .	9
1.2.0.3	David 3D Laser Scanner . . . . .	9
1.2.0.4	Handy Scan 3D . . . . .	10
<b>2</b>	<b>Structured light projection</b>	<b>11</b>
2.1	Techniques under consideration . . . . .	11
2.1.1	Moiré projection . . . . .	11
2.1.2	Microsoft Kinect . . . . .	11
2.2	Evaluation of line-scanner accuracy . . . . .	12
2.2.1	Derivation of equations . . . . .	12

2.2.2	Uncertainty of the method . . . . .	15
2.3	Evaluation of uncertainty in the moiré contouring method . . . . .	16
2.4	Uncertainty analysis . . . . .	19
2.4.1	Pixel intensity . . . . .	19
2.4.2	Pixel position . . . . .	19
2.4.3	Phase calculation . . . . .	22
2.4.3.1	Uncertainties in phase calculation . . . . .	22
2.4.3.2	Sources of phase uncertainty . . . . .	23
2.4.3.3	Sources of large error in phase calculations . . . . .	23
2.5	The correspondence problem . . . . .	23
<b>3</b>	<b>Simulation</b>	<b>24</b>
<b>4</b>	<b>Structure from motion</b>	<b>28</b>
<b>A</b>	<b>Uncertainty calculation results</b>	<b>30</b>
<b>B</b>	<b>Equipment used</b>	<b>32</b>
	<b>Bibliography</b>	<b>34</b>

# List of Figures

2.1	Setup of a line scanner. . . . .	12
2.2	Geometry in measuring one point using a line-scanning setup. . . . .	13
2.3	Triangulation geometry of a single point. . . . .	14
2.4	A computer rendering of moiré patterns on a monkey figure. . . . .	16
2.5	Schematic diagram of moiré contouring method. . . . .	18
2.6	Geometry as seen from the camera's perspective. . . . .	19
2.7	Camera geometry as seen from the top. . . . .	20
3.1	Setup of fringe simulation. . . . .	26
3.2	Output image of case (1) listed in Table 3.1 . . . . .	26
3.3	Recovered point cloud for simulation case (1). . . . .	27
4.1	Possible locations of a 3D point given fringe locations and its position in the camera view. . . . .	29
A.1	Maxima script used to calculate line-scanning triangulation uncertainty. .	31

# List of Tables

3.1	Simulation parameters. . . . .	25
3.2	Results of sphere simulation. . . . .	27
B.1	Camera properties. . . . .	32
B.2	Projector properties. . . . .	32
B.3	Motion controller properties. . . . .	33
B.4	Rotary stage properties. . . . .	33

# Nomenclature

DMD digital micro-mirror device

FPGA field-programmable data array

# Chapter 1

## Background

### 1.1 3-Dimensional Optical Shape Measurement Techniques

There are many different optical techniques for 3-Dimensional shape measurement. The different techniques each have their advantages and disadvantages, and are utilized in different professional fields. This section will give a brief overview of some of the many techniques available for 3D shape measurement.

#### 1.1.1 Photogrammetry

Photogrammetry is a technique to construct a 3D image from several 2D photos. In order to achieve this, photogrammetry utilizes feature, pattern, or color matching. Algorithms frequently use reflectivity, shading, and focus to recover shape information.[13] The advantage of this system is that it can create 3D reconstructions without knowledge of the location of the cameras. However this method has much lower accuracy than most other methods, and therefore is generally not used in engineering or medical fields.

### 1.1.2 Time of Flight

This method directly measures the time of flight of a laser or light source. The amount of time between the light being emitted, reflected off the object, and then received by the sensor is used to calculate the distance to the object.[3] Time of flight techniques have an advantage of being longer ranged than most other shape measurement techniques, but they are also lower resolution. This makes it useful for surveying, and other long range purposes.

### 1.1.3 Triangulation

Optical Triangulation techniques utilize the geometry of the system to calculate the distance from the camera to the object being measured. In most cases a projector and a camera are positioned a known distance apart. The central axis of the camera is angled by a known amount relative to the central axis of the projector. This angle is known as the triangulation angle. Triangulation techniques use these known values, along with a measured value extracted from the image data, to compute the 3D data. The most common measured values are displacement and optical phase.

#### 1.1.3.1 Laser Scanning

Laser scanning techniques work by projecting one or more laser lines on the object to be measured. The line(s) are scanned across the object while a camera captures images of the object. The camera is positioned in a known triangulation geometry with the projector. The distance to the object at each point along the line is calculated to generate a profile of the object illuminated by the line. The profiles of the line at every location as it scans across the object are combined to create a full image.[3] In order to have a resolution greater than the thickness of the laser line, an algorithm to find the center of the line can be used. (image)



### 1.1.3.2 Structured Light

Structured Light is a category of optical imaging techniques that use a coded pattern in projected light in conjunction with a camera to perform triangulation. There are two main categories of structured light techniques, which are continuous coding and discrete coding.

**Continuous Coding** Continuous coding is a term for any structured light technique that projects a continuous pattern in order to code the shape data into an image. Most continuous coding techniques utilize a sinusoidal pattern, but there are some that use other forms of continuous information. [11]

**Sinusoidal Fringe Projection** Sinusoidal Fringe Projection is the most commonly used form of continuous coding. This method utilizes a Digital Light Projector (DLP) to project vertical fringes that vary sinusoidally in intensity. To achieve this sinusoidal pattern the projector and CCD camera must be synched so that the fringes start at their maximum size and shrink to a single pixel wide during a single exposure of the camera. The intensity at each point is averaged over the exposure time so that a sinusoid is created. Four frames of data are captured, each phase shifted by a quarter of the wavelength of the sinusoid. The multiple phase shifted images are used to calculate the wrapped phase map of the object. An unwrapping algorithm gives the unwrapped phase map, and the actual size data is calculated using the triangulation geometry. [16]

**Binary Fringe Projection** Instead of a sinusoidal pattern, a binary fringe pattern is projected. This pattern is defocused to approximate a sinusoidal pattern. The phase can then be found through phase shifting in the same manner as standard sinusoidal fringe projection. The advantage of this method is that near sinusoidal fringes can be created without long exposure times and dynamic projectors. This allows for faster applications such as single frame acquisition, but reduces the accuracy of the system by

introducing higher order noise.[10]

**Fourier Transform Profilometry** Fourier Transform Profilometry is a method for calculating the wrapped phase map of the object in a single frame. The method takes the Fourier transform of the intensity and isolates the shape containing phase information. When the Fourier transform is performed, 3 distinct peaks result in the Fourier domain. The central peak is the brightness information and can be masked out. The two remaining peaks are symmetric about the origin and contain the shape information. One of these peaks is masked out, and the remaining one is shifted by the carrier frequency so it is located on the origin.[15] The inverse FFT is calculated and the phase data is separated from the contrast by taking the arc tangent of the imaginary components over the real components. [16]

**Color Coded Fringe Projection** Instead of a single fringe pattern being phase shifted between several pictures, three phase shifted patterns are projected simultaneously for single frame acquisition. These three patterns are different colors, typically RGB. The three patterns are separated and used to generate a wrapped phase map. The main limitation of this method is that it is sensitive to the transmittance, reflectivity, and absorption of the object being measured. To compensate for this the exact wavelengths used can be chosen based on the color and material of the object, or some form of coating can be applied to the object to improve the conditions. [7] (Image)

**Continuous Spatial Grading** A continuous grayscale or color scale is projected onto the object. Every X coordinate in the undistorted projection has a unique intensity value, allowing for triangulation similar to a line scanner. This method is extremely sensitive to the color of the target object and shadowing on the object. [11]

**Discrete Coding** Discrete coding consists of projecting non-continuous patterns onto an object. These patterns are designed such that every part of the image is uniquely identified by the pattern. This identification is referred to as the “codeword” for that location. The locations identified by codewords can either be lines or pixels, depending on whether the pattern is 1D or 2D. Since the location of each “codeword” is known in the projected image the displacement of the “codeword” when the pattern is projected on the object can be measured. This displacement can be used to triangulate the distance to the object for each location, thus giving the 3-dimensional shape. The two methods of discrete coding are spatial multiplexing and time multiplexing [11]

**Spatial Multiplexing** Spatial multiplexing methods project only a single pattern. In order to identify the “codewords” for that pattern, the surroundings are used. For a 1-D pattern this means the sequence of lines two either side of any given line are unique and thus identify that line. In a 2-D case it the surroundings in all directions within the plane are taken into account. [12]

**De Bruijn Coding** A pattern is constructed using a pseudorandom sequence known as a De Bruijn sequence. The properties of a De Bruijn sequence ensure that any projected line can be identified by the bordering lines, allowing for triangulation. This pattern can be binary (similar to bar code), grayscale, or color. [12] (image)

**M-Arrays** M-arrays are a 2D equivalent to the 1-D De Bruijn patterns. An array of pseudorandom dots is projected onto the target object. Any dot can be identified by the adjacent dots, allowing for triangulation. This method can utilize both binary, color or grayscale. The “codeword” of the dot can be identified not only by the type of dots around it, but by the relative density of the dots as well. [11] (image)

**Non-Formal Coding** Non-formal coding is a term used to categorize any number of spatial multiplexing methods that use unique patterns for specific purposes. These patterns do not necessarily directly uniquely identify the line or pixel as the previous methods do. Instead non-formal coding usually serves a more specific purpose such as calibration patterns. [12]

**Time Multiplexing** Time multiplexing captures successive images with different patterns in order to generate the necessary “codeword” for each location. The patterns are generated such that each location has a unique sequence of values throughout the series of images. Since multiple frames are needed to generate a 3D image, this method is not viable for high speed applications that require single frame acquisition. [11]

**Binary Codes** Binary codes function by projecting a series of binary patterns. These patterns are typically vertical of varying thicknesses or densities, similar to a bar code. A single pattern alone does nothing, but by taking into account the binary value of each line or pixel over the entire series of projected patterns, uniqueness is established. [12] (Image)

**N-Array Codes** N-Array codes utilize the same basic concept as binary codes, except they are not restricted to binary patterns. They can utilize color or grayscale patterns to greatly reduce the number of frames necessary to uniquely identify each location in the image. [12] (Image)

**Hybrid Coding** Hybrid coding consists of a combination of spatial and time multiplexing. Several spatial multiplexing patterns are displayed in series so as to create a time multiplex with them. This method achieves the high accuracy of time multiplexing, while greatly reducing the number of patterns necessary. [11]

### 1.1.4 Interferometry

Interferometry utilizes beam splitter to separate a single beam into two beams. One of the beams, the sample beam, is reflected off the target object and then into sensor. This beam then meets with the other beam, the reference beam, in an interferometer. The interference between these two beams gives the phase difference of the lasers. The phases from all the points on the object are generated into a wrapped phase map image of the object. [3]The phase maps are unwrapped, giving the shape of the object.

There are many advanced imaging techniques that use interferometry as a basis to generate absolute 3D measurements. One such technique is called laser speckle pattern sectioning. This method projects a speckle pattern on the target object which is measured using a CCD array. The pattern is scanned through a range of wavelengths. Each wavelength corresponds to a 2D slice of the 3D object. By adding these slices together into a 3D data array, and then performing a 3D Fourier transform, the 3D shape can be found. [3]

Interferometry has higher resolution and accuracy than many of the other techniques, and can be performed on a large range of object sizes depending on the setup. For this reason it can be used in a large variety fields, making it a versatile technique.[4]

## 1.2 Existing Commercial Products

There are many different commercial scanners currently on the market. Most of them cater to different professional fields and have specifications that those fields find desirable. A few of these products will be discussed in this section.

### 1.2.0.1 Kinect

The Kinect is a 3D imaging device made by Microsoft for use with their Xbox 360 gaming console. The Kinect works based on a fixed pseudorandom array of dots projected on an

infrared wavelength. The dots are formed by an array of small micro lenses, each with a slightly different focal length. The included infrared camera picks up the projection of these dots on their environment. Groups of dots are then compared against an image taken on a reference plane. Due to the pseudorandom nature of the dot array, each group is unique enough to allow identification of a particular dot based on the relative positions of neighboring dots. Furthermore, due to the different focal lengths of the micro lenses, the pattern itself will vary based on the distance between the camera and the object [6].

Microsoft has kept its specific algorithms for calculating the depth proprietary. However, the open-source community has had some success in reverse-engineering the Kinect. In its operating range between 0.8 and 3.5 meters, the Kinect can resolve depth with about 10 mm accuracy along the optical axis, and position to about 3 mm perpendicular to the optical axis [1]. (image)

### 1.2.0.2 Next Engine

Next engine is a device that projects multiple laser lines onto the target object. To construct a 3D image of an object it performs line scanning in both the vertical and horizontal directions. It takes about two minutes to create a single 3D point cloud of the object. The software that is bundled with this product has the capacity to stitch together multiple views to create full 3D images. The 3D images are in full color and can be output to several common CAD formats. The Next Engine Scanner is marketed for use in design, manufacturing, CGI, art, and medical applications. This system boasts accuracy to 0.005inches in macro mode and to 0.015inches in wide mode. [8] (image)

### 1.2.0.3 David 3D Laser Scanner

David 3D Laser Scanners come in two types. The first is a line scanning method that uses a line laser pointer and a digital camera. The laser pointer is scanned across the object

by hand while the camera captures the image data. The other scanner is a sinusoidal fringe projection system. This scanner comes with calibration patterns and a software program capable of creating and stitching 3D point clouds. The scanner has a object size range from 10mm-600mm with a accuracy up to 2% of the object size. It takes 2-4 seconds per scan and generates grayscale images. [9] (image)

#### **1.2.0.4 Handy Scan 3D**

The Handy Scan 3D scanner is a portable line scanner. It boasts an accuracy of up to 40 microns. The Handy Scan projects a cross hair onto the target object and scans in both x and y simultaneously. The device has a camera built into it so the triangulation geometry remains constant as the laser is scanned along the object. The technology requires several sensors to be placed on the object. These sensors are randomly placed on the object and are triangulated by two cameras on the scanner. This allows the scanner to know its location relative to the object, making the freehand scanning possible. This product is marketed for reverse engineering, design, and part inspection. [5] (image)

# Chapter 2

## Structured light projection

### 2.1 Techniques under consideration

#### 2.1.1 Moiré projection

#### 2.1.2 Microsoft Kinect

The Kinect works based on a fixed pseudorandom array of dots projected on an infrared wavelength. The dots are formed by an array of small microlenses, each with a slightly different focal length. The included infrared camera picks up the projection of these dots on their environment. Groups of dots are then compared against an image taken on a reference plane. Due to the pseudorandom nature of the dot array, each group is unique enough to allow identification of a particular dot based on the relative positions of neighboring dots. Furthermore, due to the different focal lengths of the microlenses, the pattern itself will vary based on the distance between the camera and the object [6].

Microsoft has kept its specific algorithms for calculating the depth proprietary. However, the open-source community has had some success in reverse-engineering the Kinect. In its operating range between 0.8 and 3.5 meters, the Kinect can resolve depth with about 10 mm accuracy along the optical axis, and position to about 3 mm perpendicular



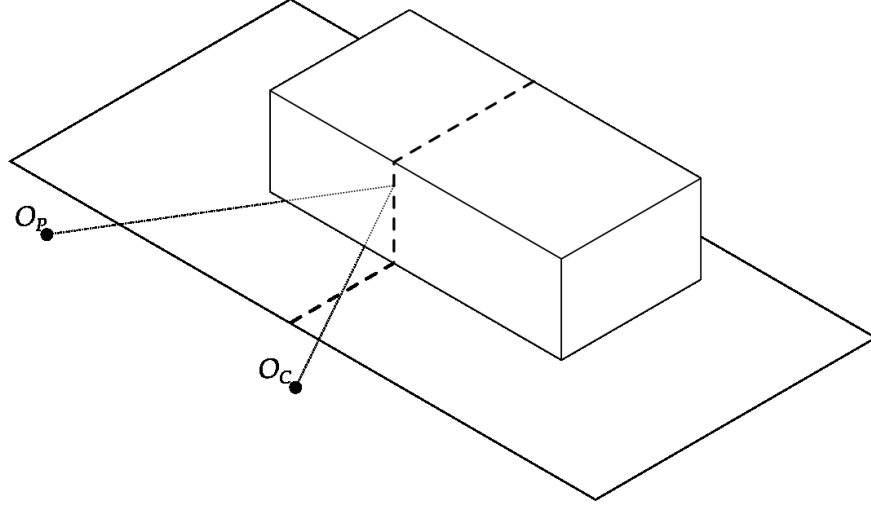


Figure 2.1: Setup of a line scanner.

to the optical axis [1].

## 2.2 Evaluation of line-scanner accuracy

One of the simplest setups to conceive and operate is a line-scanning system. Such a system projects a line, usually a laser beam, onto an object, and then uses triangulation to extract the three-dimensional data from the contour.

### 2.2.1 Derivation of equations

Figure 2.1 shows a schematic view of a single-line scanner. Point  $O_P$  denotes the source of illumination. (“P” stands for “projector”, although it could potentially be any source of illumination that conforms to the standards set forth in this document.) Point  $O_C$  denotes the camera. The dashed line laid across the object indicates the center of a single fringe, deformed by its interaction with the subject. The dotted line demonstrates the path of a particular ray of light from its emission at  $O_P$  to its absorption at  $O_C$ .

The unknowns in this set of equations can best be characterized by figure 2.2. We know that the projector will project a line on any flat surface. Extending this concept,

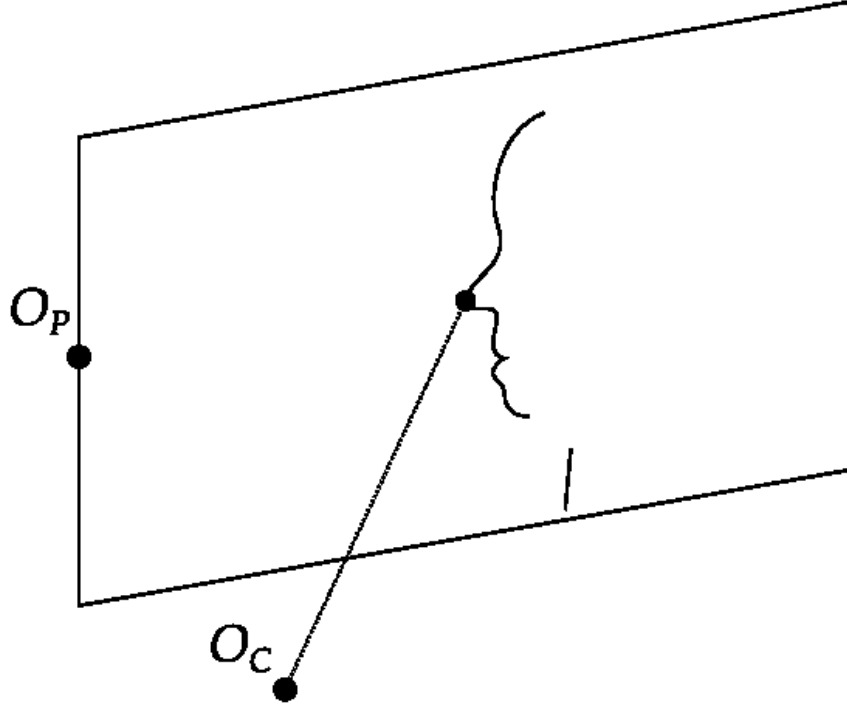


Figure 2.2: Geometry in measuring one point using a line-scanning setup.

we can imagine a “light plane” extending from the projector and intersecting the subject along its illuminated contour. We can also imagine the ray of reflected light traveling from the contour to the camera. Given the field of view of the camera, the pixel location of the illuminated point in the image, and the relative location and angle of the projector and camera, we can now compute the absolute 3D position data for the given scanned contour.

Refer to figure 2.3.  $\hat{Z}_P$  and  $\hat{Z}_C$  are defined to be the unit vectors pointing along the optical axes of the projector and camera, respectively.  $\vec{D}$  is the vector drawn from the focal point of the projector to the focal point of the camera;  $\hat{D}$  is the normalized version of this.  $\hat{M}_P$  and  $\hat{M}_C$  represent the unit vector pointing to the measured point from the projector and camera, respectively.  $\alpha_P$  is the angle between the projected ray and the projector’s optical axis; similarly,  $\alpha_C$  is the angle between the absorbed ray of light and the camera’s optical axis. The angle between the projector’s optical axis and  $\vec{D}$  will be

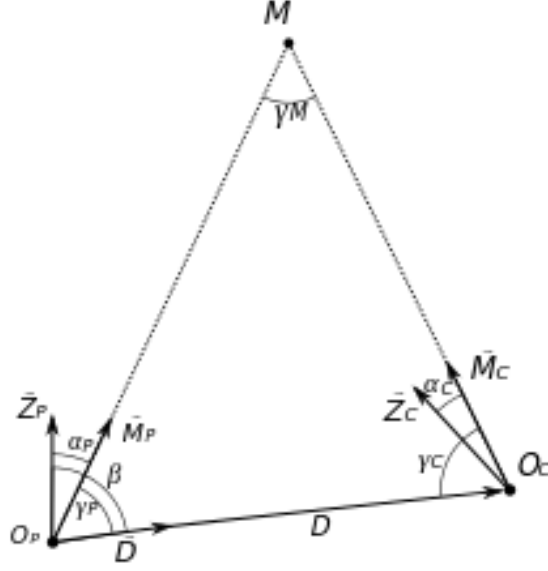


Figure 2.3: Triangulation geometry of a single point.

defined as  $\beta$ ; the angle between the projector's optical axis and camera's optical axis will be defined as  $\zeta$ . Finally,  $\gamma_P$ ,  $\gamma_M$ , and  $\gamma_C$  are the vertices of the triangle drawn between the projector, measured point, and camera, respectively.

According to the previous paragraph,

$$\alpha_P \equiv \angle(\hat{Z}_P \hat{M}_P)$$

$$\alpha_C \equiv \angle(\hat{Z}_C \hat{M}_C)$$

$$\beta \equiv \angle(\hat{Z}_P \hat{D})$$

A quick inspection of the diagram yields

$$\gamma_P = \beta - \alpha_P \tag{2.1}$$

$$\gamma_C = \alpha + \pi - \zeta - \beta \tag{2.2}$$

Combining 2.1 with 2.2 yields

$$\gamma_M = \pi - \gamma_P - \gamma_C$$

Using the law of sines,

$$M_C = \frac{D \sin \gamma_P}{\sin \gamma_C} \quad (2.3)$$

### 2.2.2 Uncertainty of the method

Uncertainty  $\sigma_y$  in a variable  $y$  is given by

$$\sigma_y = \sqrt{\left(\frac{\partial y}{\partial x_1} \sigma_{x_1}\right)^2 + \left(\frac{\partial y}{\partial x_2} \sigma_{x_2}\right)^2 + \cdots + \left(\frac{\partial y}{\partial x_n} \sigma_{x_n}\right)^2} \quad (2.4)$$

where  $y = f(x_1, x_2, \dots, x_n)$  [2, 74]. Substituting the various equations into equation 2.4, we get

$$\begin{aligned} \sigma_{\gamma_C} &= \sigma_{\alpha_C}^2 + \sigma_{\zeta}^2 + \sigma_{\beta}^2 \\ \sigma_{\gamma_P}^2 &= \sigma_{\beta}^2 + \sigma_{\alpha_P}^2 \\ \sigma \left( \frac{\sin \gamma_P}{\sin \gamma_C} \right) &= \frac{\sin \gamma_P}{\sin \gamma_C} \left[ (\sigma_{\gamma_P} \cot \gamma_P)^2 + (\sigma_{\gamma_C} \cot \gamma_C)^2 \right]^{\frac{1}{2}} \\ \sigma_{M_C} &= \frac{D \sin \gamma_P}{\sin \gamma_C} \left\{ \left( \frac{\sigma_D}{D} \right)^2 + \left[ \frac{\sin \gamma_C}{\sin \gamma_P} \sigma \left( \frac{\sin \gamma_P}{\sin \gamma_C} \right) \right]^2 \right\}^{\frac{1}{2}} \end{aligned}$$

With reasonable estimates,  $\sigma_{M_C}$  is estimated to be about 2.2 cm. The Maxima script used to calculate this is reproduced in figure A.1 on page 31.

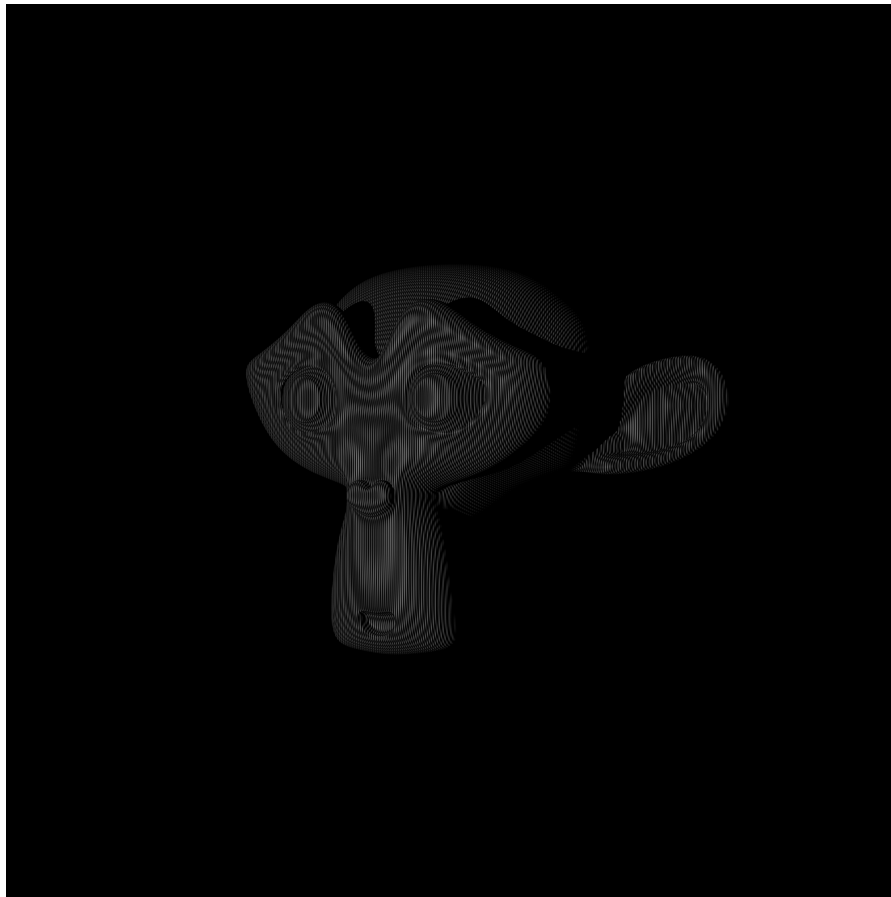


Figure 2.4: A computer rendering of moiré patterns on a monkey figure.

## 2.3 Evaluation of uncertainty in the moiré contouring method

Moiré contouring is a technique that uses interference to beautiful consequence—when light is passed through a grating, reflected off an object, and collected at a different point than where it was emitted, the entire object will appear to be wrapped in a contour map showing levels of equal displacement from the grating. Figure 2.4 displays the output of a simulated grating. The grating lines themselves are very small and can only be seen upon close inspection of the image. For instance, the gratings available in the CHSLT lab have a spacing of  $s_0 = 10 \text{ lines/mm}$ .

More importantly, assuming the camera and the light source are in the same plane

perpendicular to the fringe direction, the image shows bright contours located at points equidistant from the grating. According to [14], the  $N^{\text{th}}$  bright fringe has a depth given by

$$h = \frac{lN}{d/s_0 - N} \quad (2.5)$$

where  $l$  is the distance from the grating to the light source and camera, and  $d$  the distance between the light source and camera. If  $d \gg s_0$ , then equation 2.5 reduces to the approximation

$$h = \frac{ls_0N}{d}$$

This may be difficult to picture. Figure 2.5 demonstrates how two sets of rays through a grating produce bright equidistance contours. The circle at top-left represents a light source, and the circle at top-right a camera. In order for the camera to see a bright pixel, the following conditions have to take place:

1. The camera's view of the object at that pixel must not be impeded by the grating.
2. The object must also be lit at that location by light coming through the grating.

Using these two assumptions, we can now sketch lines through the points of maximum transmittance on the grating. Wherever these lines intersect on the object, the camera will see a bright spot.

One immediate advantage of such a simple equation is that the depths may be computed in near-real time. If the camera and light source are fixed to a rigid frame, then  $\frac{ls_0}{d}$  will be a constant. Assuming that the contour-finding algorithm is fast, the fact that the algorithm yields a fixed distance for each  $N$  will mean a computer could conceivably render a point cloud as the data comes in.

The major disadvantage of the moiré method is that it requires absolute knowledge of the contour index  $N$  for each index. These indices would be nearly impossible to guess correctly from a single view.

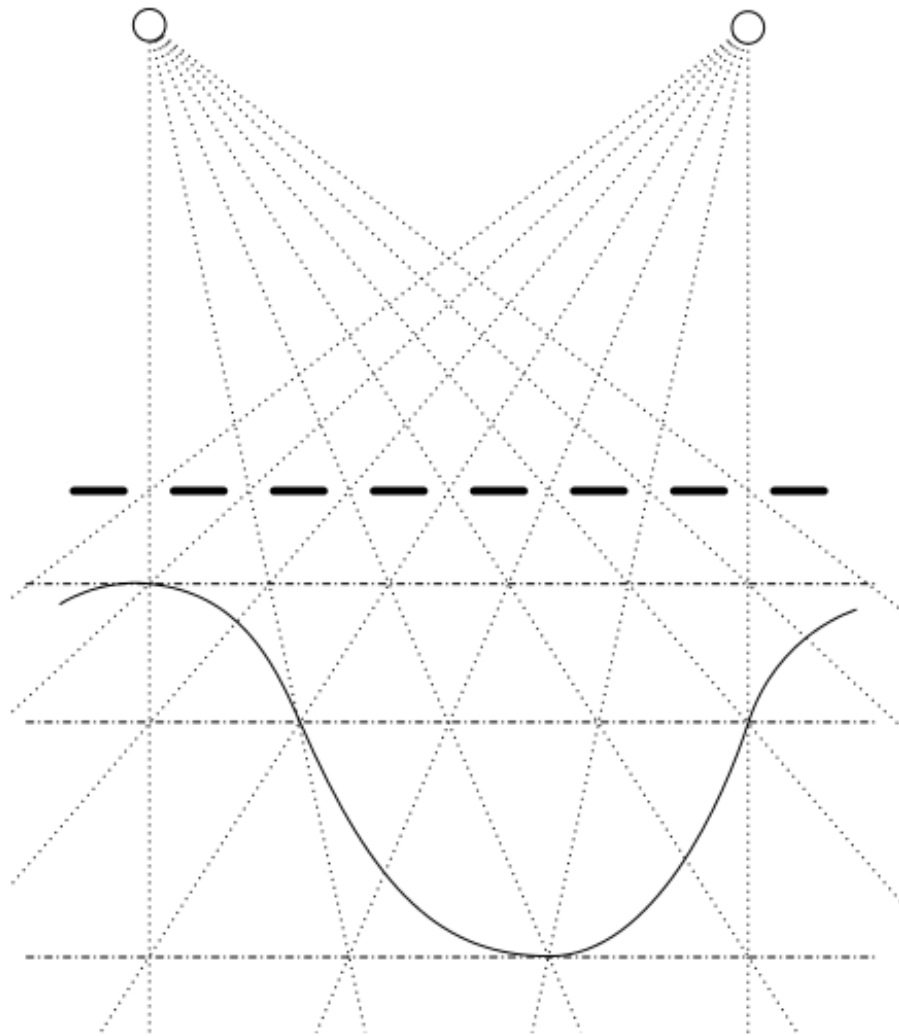


Figure 2.5: Schematic diagram of moiré contouring method.

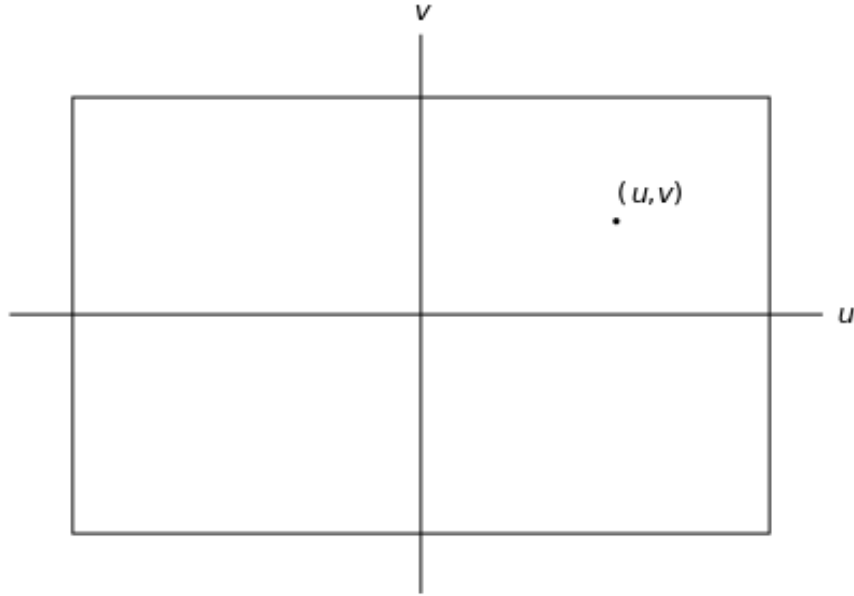


Figure 2.6: Geometry as seen from the camera's perspective.

## 2.4 Uncertainty analysis

### 2.4.1 Pixel intensity

The pixel intensity is read as an integer from the camera, which has a maximum intensity resolution of 14 bits ( $2^{14}$  or 16,384 shades of grey).

### 2.4.2 Pixel position

Define  $\beta_C$  as the horizontal lens angle of the camera, and  $R_u$  and  $R_v$  as the horizontal and vertical camera resolution, respectively. Define coordinates  $(u, v)$  in pixels (in the 2D space of the image) such that  $(u, v) = (0, 0)$  on the optical axis of the camera (i.e., in the center of the image). Define  $w$  as the optical axis itself in three-dimensional space. Let  $(u, v)$  represent the point being observed. Figure 2.6 displays the camera's view of the target pixel along with appropriately labeled axes. The rectangle represents the field of view of the camera.

Each possible set of  $(u, v)$  coordinates characterizes a ray traveling from the camera



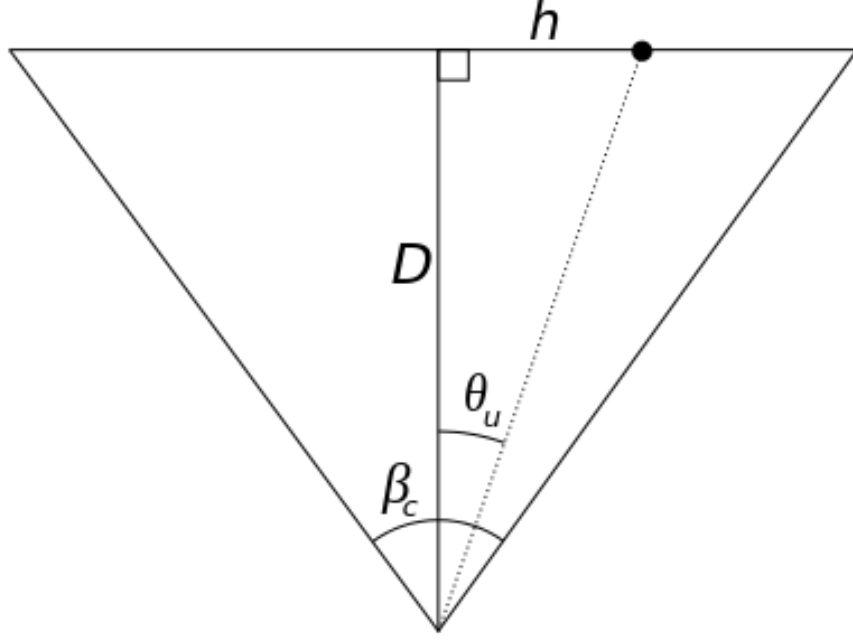


Figure 2.7: Camera geometry as seen from the top.

origin at  $O_C$  through the real point  $P$  on the object being measured. This ray may be described by two angles,  $\theta_u$  and  $\theta_v$ , measured from the ray through the planes described by  $u = 0$  and  $v = 0$ . Looking down on the system, we can now identify a working plane at a distance  $D$  from the camera origin and perpendicular to the  $w$  axis. This plane intersects the  $(u, v)$  ray at a distance  $h$  from the  $v = 0$  plane. Figure 2.7 depicts the geometry described above.

From this diagram, it becomes clear that

$$\tan \theta_u = \frac{h}{D}$$

Similarly,

$$\tan \frac{\beta_C}{2} = \frac{h_{max}}{D}$$

Solving for  $D$ , and letting  $F \equiv \tan \frac{\beta_C}{2}$  for simplicity, it follows that

$$\begin{aligned} \frac{\tan \theta_u}{h} &= \frac{F}{h_{max}} \\ \theta_u &= \arctan \left( \frac{Fh}{h_{max}} \right) \\ &= \arctan \left( \frac{2u}{R_u} F \right) \end{aligned} \tag{2.6}$$

$R_u$  has no uncertainty — it is an integer count of the physical pixels installed in the camera at the time of manufacture. For a given scanning setup, it is a constant. Therefore, all of the uncertainty arises from the field-of-view constant  $F$  and the uncertainty in the precise position of the pixel. The ideal equations assume that the ray of light passes directly through the center of the pixel, but this is not always the case. The light recorded by a given image pixel may have arrived in the center of that pixel’s collector, but it is also possible that the light arrived near the edge or near the corner.

Uncertainty  $\sigma_y$  in a variable  $y$  is given by

$$\sigma_y = \sqrt{\left( \frac{\partial y}{\partial x_1} \sigma_{x_1} \right)^2 + \left( \frac{\partial y}{\partial x_2} \sigma_{x_2} \right)^2 + \cdots + \left( \frac{\partial y}{\partial x_n} \sigma_{x_n} \right)^2}$$

where  $y = f(x_1, x_2, \dots, x_n)$  [2, 74].

Therefore the uncertainty in  $\theta_u$  is

$$\sigma_{\theta_u} = \sqrt{\left( \frac{2u}{\frac{4u^2}{R_u} F^2 - R_u} \sigma_F \right)^2 + \left( \frac{2F}{\frac{4F^2}{R_u} u^2 - R_u} \sigma_u \right)^2}$$

Assuming we can say with a 95% confidence level that the light in a given pixel “belongs in” that pixel,  $\sigma_u = 0.5\text{px}$ . Since no calibration data exists yet for the camera,  $\sigma_F$  must be estimated. For the sake of calculation, let  $\sigma_F = 0.05$ ,  $R_u = 1000\text{px}$ , and  $F = 1$  (implying  $\beta_C = 90^\circ$ ). With these assumptions, the uncertainty in  $\theta_u$  is  $25 \times 10^{-3}$  radians

on the edge of the image and  $1 \times 10^{-3}$  radians in the center.

$$\sigma_{\theta_u, max} = 25 \times 10^{-3} \text{ radians}$$

### 2.4.3 Phase calculation

There are two parts to consider in the phase calculation. First, this paper will study the translation of varying intensity levels into a phase map. Second, the validity of this phase map will be studied by assessing various contributions to variations in pixel intensity.

#### 2.4.3.1 Uncertainties in phase calculation

The wrapped phase may be calculated as

$$\phi = \arctan \left( \frac{-\sum_{i=1}^m I_i \sin [\alpha (i - 1)]}{\sum_{i=1}^m I_i \cos [\alpha (i - 1)]} \right)$$

([16], 32). This assumes that the induced phase shift is evenly spaced across the full set of  $m$  images, which allows for the most accurate calculation of applied phase. For convenience we will define  $\alpha_i \equiv \alpha (i - 1)$ .

The uncertainty in the wrapped phase calculation is given as

$$\left( \frac{\sigma_\phi}{\phi} \right)^2 = \left[ \frac{\sum \sigma_{I_i} \sin \alpha_i}{\sum I_i \sin \alpha_i} + \frac{\sum \sigma_{I_i} \cos \alpha_i}{\sum I_i \cos \alpha_i} + 1 \right]^{-2}$$

in which each summation is taken from  $i = 1 \rightarrow m$ .

### 2.4.3.2 Sources of phase uncertainty

Uncertainty in an intensity level due to bit depth is inversely exponentially proportional to the bit depth  $B_C$  of the camera:

$$\sigma_{I,B} = 2^{-B_C}$$

### 2.4.3.3 Sources of large error in phase calculations

Certain factors can create unnecessary and uncontrolled error in phase calculations. The most significant such factor is an overexposed image. By maxing out the camera's ability to detect light over part of the fringe-shifting process, a bright surface can tend to generate certain phases dictated only by induced phase shift and not at all by the surface's location. Furthermore, by overexposing the camera even without fringes projected, bright light can completely remove all meaningful information from a projected view.

## 2.5 The correspondence problem

It is a simple matter to project a single fringe upon an object and triangulate.

# Chapter 3

## Simulation

In order to gauge the accuracy of the technique, a simulation was developed using Blender<sup>1</sup>, an open-source 3D graphics program. Blender allows full control over most parameters, including field-of-view and positioning of the camera and projector.

To allow for simple quantitative evaluation, a sphere was first chosen as the simulated object. Table 3.1 shows the parameters set for the simulation. The distance from the point light source to the fringe plane is 10 cm in all cases.

Figure 3.1 shows the setup, with the results from a single-fringe scan superimposed in orange. Figure 3.2 shows the image output of the first case listed in the parameter table.

---

<sup>1</sup><http://www.blender.org>

Case	$D$ (m)	$\psi$ (degrees)	$W_{fringe}$ (mm)	$O_R$	$r_{sphere}$ (mm)	$f$ (mm)	$R$ ( $\mu\text{m}/\text{px}$ )	$S_{image}$ (px)
1	$\begin{pmatrix} -0.3 \\ 0 \\ 0 \end{pmatrix}$	17	2	$\begin{pmatrix} 0 \\ 0 \\ 1 \end{pmatrix}$	30	38.627	32	$\begin{pmatrix} 1000 \\ 1000 \end{pmatrix}$
2	$\begin{pmatrix} -0.3 \\ 0 \\ 0 \end{pmatrix}$	17	0.5	$\begin{pmatrix} 0 \\ 0 \\ 1 \end{pmatrix}$	30	38.627	32	$\begin{pmatrix} 1000 \\ 1000 \end{pmatrix}$
3	$\begin{pmatrix} -0.3 \\ 0 \\ 0 \end{pmatrix}$	17	1	$\begin{pmatrix} 0 \\ 0 \\ 1 \end{pmatrix}$	30	38.627	32	$\begin{pmatrix} 1000 \\ 1000 \end{pmatrix}$

Table 3.1: Simulation parameters.

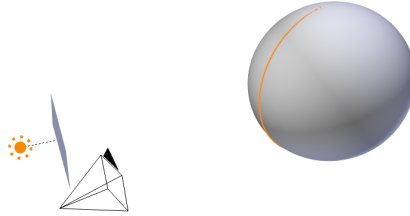


Figure 3.1: Setup of fringe simulation.

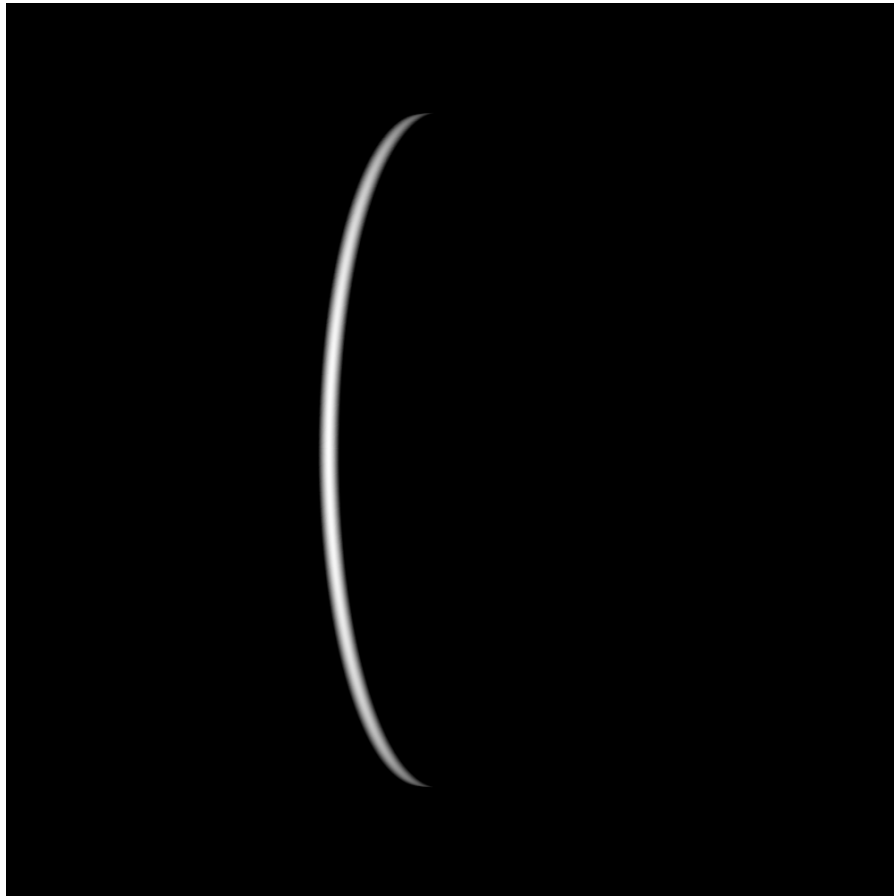


Figure 3.2: Output image of case (1) listed in Table 3.1

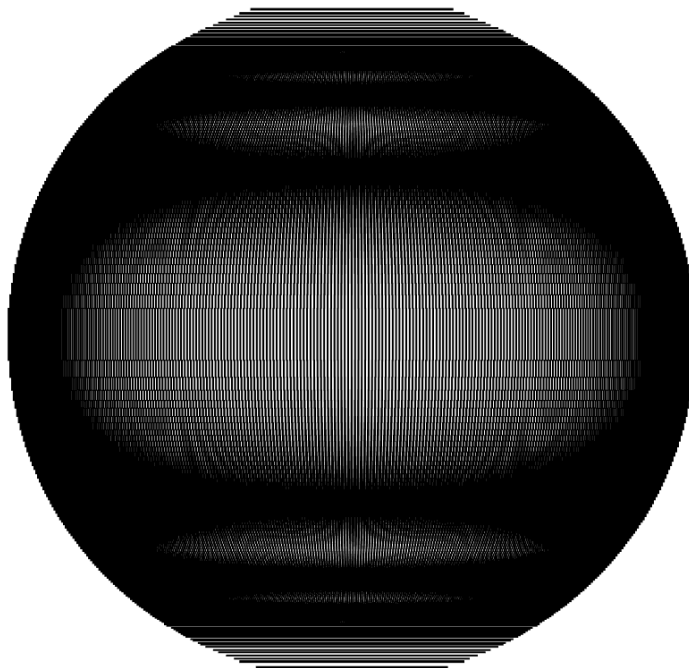


Figure 3.3: Recovered point cloud for simulation case (1).

Case	Average recovered radius (mm)	RMS error	
		$\mu\text{m}$	%
1	300.012	510.083	0.1700
2	300.097	509.493	0.1698
3	299.988	490.048	0.1633

Table 3.2: Results of sphere simulation.



# Chapter 4

## Structure from motion

The premise of this technique relies on the computer's ability to test many "theories" in a brief span of time.

For a given series of fringes, camera/projector relationship, rotary stage position  $\rho$ , and selected illuminated point  $(u, v)$ , there is a number  $N$  of possible points  $X$  which corresponds to the number of fringes being projected. Each of these possibilities is calculated and stored; it can be recalled by a function  $X(\rho, u, v, n)$  of the rotary stage position  $\rho$  when the video frame was taken, the image coordinates  $(u, v)$ , and the predicted fringe index  $n$ . It is a difficult problem to calculate from a single frame which fringe a pixel "belongs" to. Figure 4.1 demonstrates the geometry. Of course, given initial conditions such as rough diameter and height of the object, it is possible to "throw out" points with too great an  $r$  or  $z$ . It is also possible to rule out possibilities by the fringes visible in the video frame. For example, if an illuminated pixel has 8 fringes to the left and 12 to the right, we can be certain that  $8 < n < N - 12$ .

The computer maintains a list of each point in cylindrical coordinates, storing  $(r, \theta, z)$  for every potential match along with an ID. This ID  $i$  is unique to each potential point  $X$ . As the object rotates, the given point  $M$  on the object will come into view again, this time illuminated by a different fringe. A new set is constructed. Again, this set

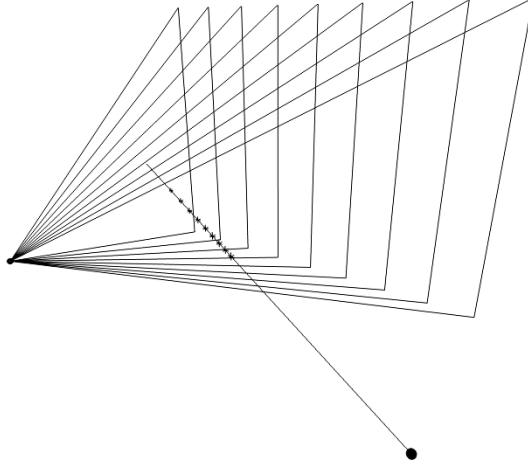


Figure 4.1: Possible locations of a 3D point given fringe locations and its position in the camera view.

may be simplified by removing impossible points.

Each frame, characterized by its stage rotation  $\rho$ , will generate a point cloud  $X(u, v, n)$  which is a set of points whose members may be uniquely identified by their image position  $(u, v)$  and their guessed fringe index  $n$ . These potential points will be added to the general cloud of potential points  $X$ . This will contain the actual measurements, but these will be buried since only 1 in  $N$  points will represent the object.

To sort these out, we check each point  $(r, \theta, z)$  in the cloud. Each of these points will be represented multiple times, but each representation will have a fixed relationship between  $\rho$  and  $n$ . In other words, given a point  $(r, \theta, z)$  on the object and the stage rotation  $\rho$ , we can calculate the expected fringe index  $n$ ; likewise, given a fringe index we can calculate the necessary stage rotation. Each of the points in the potential cloud will therefore be characterized by five coordinates  $(r, \theta, z, \rho, n)$ .

# Appendix A

## Uncertainty calculation results

```

(%i1) numer:true$
      set_display('none)$
(%i3) sigma_gamma_c:=sqrt(
      sigma_alpha_c^2+sigma_zeta^2+
      sigma_beta^2)$
sigma_gamma_p:=sqrt(sigma_beta^2+sigma_alpha_p^2)$
sigma_sinsin:=(sin(gamma_p)/sin(gamma_c))*
      sqrt(
      (sigma_gamma_p*cot(gamma_p))^2+
      (sigma_gamma_c*cot(gamma_c))^2
      )$
sigma_M_c:=D*sin(gamma_p)/sin(gamma_c)*
      sqrt(
      (sigma_D/D)^2+
      (sigma_sinsin()*sin(gamma_c)/sin(gamma_p))^2
      )$
(%i7) sigma_alpha_c : 0.01*%pi/180 $
sigma_zeta : 0.10*%pi/180 $
sigma_beta : 0.10*%pi/180 $
sigma_alpha_p : 1.2*%pi/180 $
sigma_D : 0.01*m $

gamma_p : 45*%pi/180 $
gamma_c : 90*%pi/180 $
D : 1.40*m $
(%i15) sigma_M_c();
(%o15) 0.021974106432729*m

```

Figure A.1: Maxima script used to calculate line-scanning triangulation uncertainty.

# Appendix B

## Equipment used

**Camera** The camera is an Allied Vision Technologies Pike F-100B. Specifications are listed in table B.1.

Resolution	$1000 \times 1000$
Frame rate	Up to 60 fps
Bit depth	Up to 16 bits/pixel
Peak sensor efficiency wavelength	About 450 nm
Sensor cell size	$7.4 \mu\text{m}$

Table B.1: Camera properties.

**DMD projector** The DMD projector under consideration is a Vialux projector containing a light-emitting diode (LED) of model LED-OM HP-95-R. Specifications are listed in table B.2.

Power	30 mW
Center wavelength	624 nm
Resolution	1080p ( $1920 \times 1080$ pixels)

Table B.2: Projector properties.

**Projector controller** The projector controller is a D4100 Explorer FPGA (field-programmable gate array).

**Stage controller** The stage controller is a Newport Universal Motion Controller/-Driver, Model ESP300. Specifications are listed in table B.3.

Communication rate	19200 bits/s
Byte size	8 bits
Parity	None
Stop bits	1

Table B.3: Motion controller properties.

**Rotary stage** The rotary stage is an Aerotech ART330-G108 Rotary Stage. Specifications are listed in table B.4.

Gear ratio	108:1
Stage diameter	30 cm
Resolution	3 arcsec at 4000 $\text{steps}/\text{rev}$
Accuracy	0.5 arcsec
Precision	6 arcsec

Table B.4: Rotary stage properties.

# Bibliography

- [1] Imaging information.
- [2] Thomas G. Beckwith, Roy D. Marangoni, and John H. Lienhard V. *Mechanical Measurements*. Prentice Hall, 6 edition, 2007.
- [3] Frank Chen, Gordon M. Brown, and Mumin Song. Overview of three-dimensional shape measurement using optical methods. *Optical Engineering*, 39(1):10–22, 2000.
- [4] Z Corperation. 3d scanners: Selection criteria for common applications. Technical report, T. A. Grimm and Associates Inc.
- [5] Creaform. Handy scan 3d. Online, 2012.
- [6] Barak Freedman, Alexander Shpunt, Meir Machline, and Yoel Arieli. Depth mapping using projected patterns, 2009.
- [7] P.S. Huang, Q. Hu, F. Jin, and F.P. Chiang. Color-encoded digital fringe projection technique for high-speed three-dimensional surface contouring. *Optical Engineering*, 38(6):1065–1071, 1999.
- [8] NextEngine Inc. Next engine. Online, 2012.
- [9] David LaserScanner. David laserscanner. Online, 2012.

- [10] S. Lei and S. Zhang. Digital sinusoidal fringe pattern generation: defocusing binary patterns vs focusing sinusoidal patterns. *Optics and Lasers in Engineering*, 48(5):561–569, 2010.
- [11] J. Salvi, S. Fernandez, T. Pribanic, and X. Llado. A state of the art in structured light patterns for surface profilometry. *Pattern recognition*, 43(8):2666–2680, 2010.
- [12] J. Salvi, J. Pages, and J. Batlle. Pattern codification strategies in structured light systems. *Pattern Recognition*, 37(4):827–849, 2004.
- [13] K. N. Snavely. *Scene reconstruction and visualization from internet photo collections*. PhD thesis, University of Washington, 2008.
- [14] H. Takasaki. Moiré topography. *Appl. Opt.*, 9(6):1467–1472, Jun 1970.
- [15] Mitsuo Takeda and Kazuhiro Mutoh. Fourier transform profilometry for the automatic measurement of 3-d object shape. *Appl. Opt.*, 22(24):3977–3982, Dec 1983.
- [16] Michael J. Zervas. Development of a high-speed, robust system for full field-of-view 3d shape measurements. Master’s thesis, Worcester Polytechnic Institute, August 2011.